Heat transfer and fluid flow during electron beam welding of 21Cr–6Ni–9Mn steel and Ti–6Al–4V alloy

R Rai[1], P Burgardt[2], J O Milewski[2], T J Lienert[2] and T DebRoy[1]

[1] Department of Materials Science and Engineering, The Pennsylvania State University, University Park, PA 16802, USA
[2] Materials Science and Technology: Metallurgy Group, Los Alamos National Laboratory, Los Alamos, NM 87545, USA

Abstract
Electron beam welding (EBW) of two important engineering alloys, Ti–6Al–4V and 21Cr–6Ni–9Mn, was studied experimentally and theoretically. The temperatures at several monitoring locations in the specimens were measured as a function of time during welding and the cross-sections of the welds were examined by optical microscopy. The theoretical research involved numerical simulation of heat transfer and fluid flow during EBW. The model output included temperature and velocity fields, fusion zone geometry and temperature versus time results. The numerically computed fusion zone geometry and the temperature versus time plots were compared with the corresponding experimentally determined values for each weld. Both the experimental and the modelling results were compared with the corresponding results for the keyhole mode laser beam welding (LBW).

Both experimental and modelling results demonstrate that the fusion zone size in Ti–6Al–4V alloy was larger than that of the 21Cr–6Ni–9Mn stainless steel during both the electron beam and laser welding. Higher boiling point and lower solid state thermal conductivity of Ti–6Al–4V contributed to higher peak temperatures in Ti–6Al–4V welds compared with 21Cr–6Ni–9Mn stainless steel welds. In the EBW of both the alloys, there were significant velocities of liquid metal along the keyhole wall driven by the Marangoni convection. In contrast, during LBW, the velocities along the keyhole wall were negligible. Convective heat transfer was important in the transport of heat in the weld pool during both the laser and the EBW. The computed keyhole wall temperatures during EBW at low pressures were lower than those during the LBW at atmospheric pressure for identical heat input.

(Some figures in this article are in colour only in the electronic version)

1. Introduction

High energy density heat sources such as electron beams or laser beams are often used when deep penetration welds with small heat affected zones (HAZs) are desired. The intense evaporation of the metal often results in the formation of a deep and narrow vapour cavity within the molten weld pool known as the 'keyhole' [1, 2]. Numerical modelling of heat transfer and fluid flow in keyhole mode welding processes can provide quantitative information about the weld geometry, thermal cycles, cooling rates and solidification characteristics.

Recent work has also shown that phenomenological models, once validated with experimental data, can also serve as powerful tools for tailoring weld attributes based on scientific principles. Several numerical models for keyhole mode laser beam welding (LBW) and electron beam welding (EBW) are available in the literature [3–27]. Models for keyhole mode laser welding range from the ones that neglect convective heat flow to the ones that solve three-dimensional heat transfer and fluid flow along with tracking of the liquid–vapour interface. On the other hand, even though numerical studies for keyhole mode electron beam welds have been reported [24–28], no

phenomenological model considering three-dimensional heat transfer and fluid flow for EBW has been reported in any peer reviewed journal. Wei and Giedt [24] proposed a 2D heat transfer and fluid flow model and computed the free surface temperature, liquid layer thickness and tangential free surface fluid velocities. Elmer *et al* [25] proposed the use of three different heat transfer models based on point, line and distributed heat sources depending on the input power and input power density. Wei and Chow [26] modelled EBW assuming circular cross-section of keyhole and neglecting latent heat due to melting and evaporation, radiative loss and convection in melt pool. Keyhole surface temperatures were calculated through a balance between surface tension and vapour pressure. The computed keyhole surface temperatures for Al 1100 alloy varied with depth by as much as 600 K. Ho *et al* [27] calculated the keyhole wall temperatures using a three-dimensional analytical model assuming the keyhole shape to be a paraboloid of revolution. They neglected fluid flow calculations and instead enhanced the thermal diffusivity by five times the molecular value to account for convective heat transfer. Hemmer and Grong [28] proposed an analytical heat conduction model and predicted keyhole penetration assuming a cylindrical keyhole shape with a predefined surface temperature. These available models of keyhole mode electron beam welding simplified the problem by using a two-dimensional approximation to a three-dimensional problem [24], neglecting fluid flow [25, 27, 28], considering a predefined keyhole shape [26–28] and/or surface temperature [28].

Although both the laser beams and electron beams are used for deep penetration welds, there are important differences in the two welding processes. LBW is generally conducted at atmospheric pressure whereas the EBW is commonly conducted under vacuum levels of about 10^{-5} Torr. Within the keyhole, the pressure exerted by metal vapours on the wall balances the pressure due to surface tension, hydrostatic and capillary forces. As these forces vary with depth, the equilibrium wall temperature also varies with depth. Assuming that the keyhole is filled with metal vapours, the variation of wall temperature with depth in laser welding is likely to be small compared with the variation in EBW (see appendix). In laser welding, the temperature on the keyhole walls is often assumed to be equal to the normal boiling point of the alloy at all depths [17–23]. On the other hand, during EBW conducted under typical vacuum levels, there can be significant variation of wall temperatures with depth [26, 29]. The variation of temperature on the keyhole walls in EBW results in Marangoni convection currents along the keyhole walls and affects convective heat transfer within the weld pool.

When a laser or electron beam is incident on the keyhole walls at small angles, only a small portion is absorbed by the material while the remainder is reflected from the point of incidence [30]. The reflected beam strikes the keyhole at a different location and gets partially absorbed. Multiple reflections [14–17, 19–23] of the beam in the keyhole enhance the absorption of the laser or electron beam by the workpiece during the keyhole mode welding process. The enhancement of absorption due to multiple reflections has been treated in the literature by ray-tracing techniques [16]. Accuracy of the ray-tracing approach depends on the number of rays tracked and the keyhole geometry. Kaplan [17] proposed a more efficient algorithm where an average location independent enhanced absorption coefficient can be analytically deduced based on the normal absorption coefficient and the average number of reflections of the beam inside the keyhole considering both the principle of multiple reflections and the keyhole geometry. In this work, the latter approach has been followed.

Here we develop and test a three-dimensional numerical model of heat transfer and fluid flow in keyhole mode EBW. The model takes into account the variation of wall temperature with depth and Marangoni convection on keyhole walls. Experimental work involved EBW of Ti–6Al–4V and 21Cr–6Ni–9Mn steel at two power levels. The temperatures at several monitoring locations in the specimens were measured as a function of time during welding and the cross-sections of the welds were examined by optical microscopy. The numerically computed fusion zone geometry and the temperature versus time plots were compared with the corresponding experimentally determined values for each weld. A limited number of keyhole mode LBW experiments were undertaken to show the agreement between experimentally observed weld dimensions and the values calculated assuming a constant temperature on the keyhole walls. The weld geometries calculated for LB welds at atmospheric pressure and EB welds at near-vacuum conditions, under similar process parameters were subsequently compared.

2. Experiments

Electron beam welds were made on 21Cr–6Ni–9Mn stainless steel and Ti–6Al–4V samples at 16.9 mm s^{-1} welding speed and different power levels. The sample thickness was 6.45 mm for stainless steel and 7.13 mm for Ti–6Al–4V. Several laser beam welds were also made on these alloys for comparison. The composition of 21Cr–6Ni–9Mn stainless steel was 18.9% Cr, 7.4% Ni, 8.8% Mn, 0.47% Si, 0.26% N, 0.014% Al, <0.005% O, <0.01% P and balance Fe. The composition of Ti–6Al–4V alloy was 6.0% Al, 4.2% V, 0.014% C, 0.11% O, 0.17% Fe, <0.003% B, <0.03% Si, 0.0028% H, 0.005% Y and balance Ti.

For EBW, the work distance was 244.5 mm (9.625″) and chamber pressure was about 4×10^{-5} Torr. The electron beam currents were 3.7 and 7.4 mA for 21Cr–6Ni–9Mn stainless steel and 5.0 and 10.0 mA for Ti–6Al–4V, at 110 kV. Four 0.2 mm diameter type K thermocouples were used to record thermal cycles. The thin thermocouples were chosen to accurately record the rapid temperature changes. The thermocouples were spot welded at (i) $y = +1.5$ mm, top surface, (ii) $y = -1.5$ mm, top surface, (iii) $y = 2.5$ mm, top surface and (iv) $y = 0$ mm, bottom surface where y indicates the distance from the weld centre line. The plate was clamped on the four corners with a 6.35 mm (0.25″) space under each corner in order to thermally isolate the bottom of the plate from the holding fixture. The electron beam radius at sharp focus

was measured to be about 0.12 mm for 21Cr–6Ni–9Mn steel welds and 0.13 mm for Ti–6Al–4V alloy welds.

Laser beam welds were made on both materials with the Nd : YAG laser with a focal spot radius of about 0.18 mm with a divergence of 0.045 mm mm^{-1} (increase in radius per millimetre of penetration) at input power of 1500 W and welding speed of 16.9 mm s^{-1}. The laser beam was focused at 0.127 mm below the workpiece surface for 21Cr–6Ni–9Mn stainless steel and focused on the workpiece surface for Ti–6Al–4V weld.

3. Mathematical model

3.1. Calculation of keyhole profile

The welding process is assumed to be quasi-steady state with a flat top surface except where the keyhole is formed. The fluctuations of the keyhole shape and size have been neglected. The keyhole geometry is calculated using a model that considers the energy balance on the liquid–vapour interface. While the keyhole wall temperature is commonly assumed to be equal to the boiling point of the alloy for LBW [17, 19–23], the temperature on the keyhole walls in EBW is calculated from the local pressure in the keyhole. The normal boiling point of the alloy was taken to be a temperature where the sum total of the equilibrium vapour pressures of all alloying elements over the alloy added up to 1 atm. Since the orientation of the keyhole is almost vertical and the temperature gradient in the vertical direction is very small compared with the temperature gradient in the horizontal plane, the heat transfer takes place mainly along horizontal planes. During calculation of the asymmetric geometry of the keyhole, all temperatures inside the keyhole were assigned the wall temperature at that depth, for the identification of the keyhole. At each horizontal *xy* plane, the keyhole boundary was identified by both a minimum *x* value and a maximum *x* value for any *y* value where *x* is the direction of welding. Data used in the calculations are given in tables 1 and 2 [31–41]. The absorption of laser radiation in the plasma phase has been modelled previously [42–44]. The attenuation of the beam as it traverses a unit distance in the plasma is sometimes estimated by using attenuation coefficients [17] based on prior experimental and theoretical results. Some of the incident beam is absorbed or scattered by metal vapours and plasma in the keyhole region. Scattering of a laser or an electron beam by a plasma may result in refocusing of the beam and, consequently, a change in spot radius at the workpiece surface [45]. In an electron beam, large angle backscattering of electrons by the plasma can also result in some power loss but is assumed to be small for high voltage electron beams [30]. With a plasma attenuation coefficient value of 10/m used for the electron beam plasma here, 99% and 96% of the electron beam passes through lengths 1 mm and 4 mm, respectively, of the plasma.

3.2. Heat transfer and fluid flow in the weld pool

After calculating the keyhole profile, the fluid flow and heat transfer in the weld pool is modelled by solving the equations of conservation of mass, momentum and energy

Table 1. Data used for keyhole calculations.

Physical property	21–6–9 SS	Ti–6Al–4V
Boiling point at 1 atm, (K) [31]	2881	3315
Density of liquid at boiling point, (kg m^{-3}) [31–34]	5800	3780
Specific heat of liquid at boiling point, (J kg^{-1} K^{-1}) [31, 32, 35–37]	800	730
Thermal conductivity of liquid at boiling point, (W m^{-1} K^{-1}) [32, 36, 38–40]	32	37
Laser beam absorption coefficient, η	0.24	0.24
Electron beam absorption coefficient, η [30]	0.25	0.25
Change in laser beam radius with depth, (mm mm^{-1})	0.045	0.045
Change in electron beam radius with depth, (mm mm^{-1})	0.00	0.00
Plasma attenuation coefficient for laser, (m^{-1}) [23]	100	100
Plasma attenuation coefficient for e-beam, (m^{-1})	10	10

Note: Values are estimates based on the data available in the references.

Table 2. Data used for fluid flow calculations.

Physical property	21–6–9 SS	Ti–6Al–4V
Solidus temperature, (K) [35, 41]	1697	1878
Liquidus temperature, (K) [35, 41]	1727	1928
Density of liquid (kg m^{-3}) [31, 41]	7000	4000
Specific heat of solid, (J kg^{-1} K^{-1}) [31, 41]	712	670
Specific heat of liquid, (J kg^{-1} K^{-1}) [31, 41]	800	730
Thermal conductivity of liquid, (W m^{-1} K^{-1}) [32, 36, 38–40]	29	29
Thermal conductivity of solid, (W m^{-1} K^{-1}) [32, 36, 38–40]	29	21
Viscosity, (Pa-s)[35,41]	0.007	0.005
Coefficient of thermal expansion, (1/K) [31]	1.96×10^{-5}	8×10^{-6}
Temperature coefficient of surface tension, (N m^{-1} K^{-1}) [30, 34]	-0.43×10^{-3}	-0.26×10^{-3}
Enthalpy of solid at melting point, (J kg^{-1}) [31, 35]	1.20×10^{6}	1.12×10^{6}
Enthalpy of liquid at melting point, (J kg^{-1}) [31, 35]	1.26×10^{6}	1.49×10^{6}
Emissivity	0.3	0.2
Heat transfer coefficient, W m^{-2} K^{-1}	210	210

Note: Values are estimates based on the data available in the references.

in three dimensions. The molten metal is assumed to be incompressible. The liquid metal flow in the weld pool can be represented by the following momentum conservation equation [46, 47]:

$$\rho \frac{\partial u_j}{\partial t} + \rho \frac{\partial (u_i u_j)}{\partial x_i} = \frac{\partial}{\partial x_i} \left(\mu \frac{\partial u_j}{\partial x_i} \right) + S_j, \qquad (1)$$

where ρ is the density, t is the time, x_i is the distance along the ith ($i = 1, 2$ and 3) orthogonal direction, u_j is the velocity component along the j direction, μ is the effective viscosity, and S_j is the source term for the jth momentum equation and
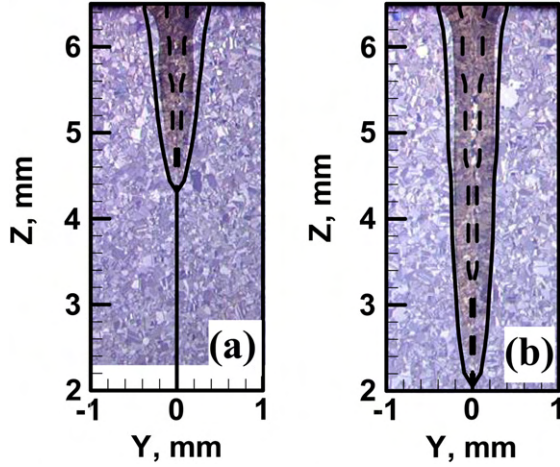
Figure 1. Comparison of the experimentally determined and computed electron beam fusion zone cross-section for 21Cr–6Ni–9Mn stainless steel at $16.9 \, \text{mm s}^{-1}$ welding speed and at input powers (*a*) 407 W and (*b*) 814 W. The computed fusion zone and keyhole geometries are shown by solid lines and dashed lines, respectively.

is given as

$$S_j = -\frac{\partial p}{\partial x_j} + \frac{\partial}{\partial x_i}\left(\mu \frac{\partial u_i}{\partial x_j}\right) - C\left(\frac{(1-f_L)^2}{f_L^3 + B}\right)u_j$$
$$+ \rho g_j \beta(T - T_{\text{ref}}) - \rho U \frac{\partial u_j}{\partial x_1}, \tag{2}$$

where p represents pressure, U is the welding velocity and β is the coefficient of volume expansion. The third term represents the frictional dissipation in the mushy zone according to the Carman–Kozeny equation for flow through a porous media [48, 49], where f_L is the liquid fraction, B is a very small computational constant introduced to avoid division by zero and C is a constant accounting for the mushy zone morphology (a value of 1.6×10^4 was used in the present study [49]). The fourth term is the buoyancy source term [50–54]. The last term accounts for the relative motion between the electron beam and the workpiece [50].

The following continuity equation is solved in conjunction with the momentum equation to obtain the pressure field:

$$\frac{\partial(\rho u_i)}{\partial x_i} = 0. \tag{3}$$

In order to trace the weld pool liquid/solid interface, i.e. the phase change, the total enthalpy H is represented by a sum of sensible heat h and latent heat content ΔH, i.e. $H = h + \Delta H$ [50]. The sensible heat h is expressed as $h = \int C_p \, dT$, where C_p is the specific heat and T is the temperature. The latent heat content ΔH is given as $\Delta H = f_L L$, where L is the latent heat of fusion. The liquid fraction f_L is assumed to vary linearly with temperature for simplicity [50]:

$$f_L = \begin{cases} 1 & T > T_L, \\ \dfrac{T - T_S}{T_L - T_S} & T_S \leqslant T \leqslant T_L, \\ 0 & T < T_S, \end{cases} \tag{4}$$

where T_L and T_S are the liquidus and solidus temperatures, respectively. Thus, the thermal energy transportation in the weld workpiece can be expressed by the following modified energy equation:

$$\rho \frac{\partial h}{\partial t} + \rho \frac{\partial(u_i h)}{\partial x_i} = \frac{\partial}{\partial x_i}\left(\frac{k}{C_p}\frac{\partial h}{\partial x_i}\right) + S_h, \tag{5}$$

where k is the thermal conductivity. The source term S_h is due to the latent heat content and is given as

$$S_h = -\rho \frac{\partial(\Delta H)}{\partial t} - \rho \frac{\partial(u_i \Delta H)}{\partial x_i} - \rho U \frac{\partial h}{\partial x_i} - \rho U \frac{\partial \Delta H}{\partial x_1}. \tag{6}$$

The heat transfer and fluid flow equations were solved [47] for the entire workpiece. Since the keyhole does not contain any liquid, liquid metal velocities within the keyhole were assigned zero values and the temperatures inside the keyhole were taken as the boiling point of the alloy.

3.2.1. Boundary conditions. A 3D Cartesian coordinate system is used in the calculation, and only half of the workpiece is considered since the weld is symmetrical about the weld centre line. The boundary conditions are discussed as follows.

Top surface. The weld top surface is assumed to be flat, except for the keyhole region. The velocity boundary conditions are given as [53–57]

$$\mu \frac{\partial u}{\partial z} = f_L \frac{d\gamma}{dT}\frac{\partial T}{\partial x},$$
$$\mu \frac{\partial v}{\partial z} = f_L \frac{d\gamma}{dT}\frac{\partial T}{\partial y}, \tag{7}$$
$$w = 0,$$

where u, v and w are the velocity components along the x, y and z directions, respectively, and $d\gamma/dT$ is the temperature coefficient of surface tension. As shown in this equation, the u and v velocities are determined from the Marangoni effect [53–57]. The w velocity is equal to zero since the outward flow at the pool top surface is assumed to be negligible.

The heat flux at the top surface is given as

$$k\frac{\partial T}{\partial z}\bigg|_{\text{top}} = \frac{fQ\eta}{\pi r_b^2}\exp\left(-\frac{f(x^2 + y^2)}{r_b^2}\right)$$
$$-\sigma\varepsilon(T^4 - T_a^4) - h_c(T - T_a), \tag{8}$$

where r_b is the beam radius, f is the power distribution factor, Q is the total laser power, η is the absorptivity, σ is the Stefan–Boltzmann constant, h_c is the heat transfer coefficient and T_a is the ambient temperature. In equation (8), the first term on the right-hand side is the heat input from the Gaussian heat source. The second and third terms represent the heat loss by radiation and convection, respectively.

Symmetric plane. The boundary conditions are defined as zero flux across the symmetric surface, i.e. the vertical plane defined by the welding direction, as

$$\frac{\partial u}{\partial y} = 0, \qquad v = 0, \qquad \frac{\partial w}{\partial y} = 0, \tag{9}$$

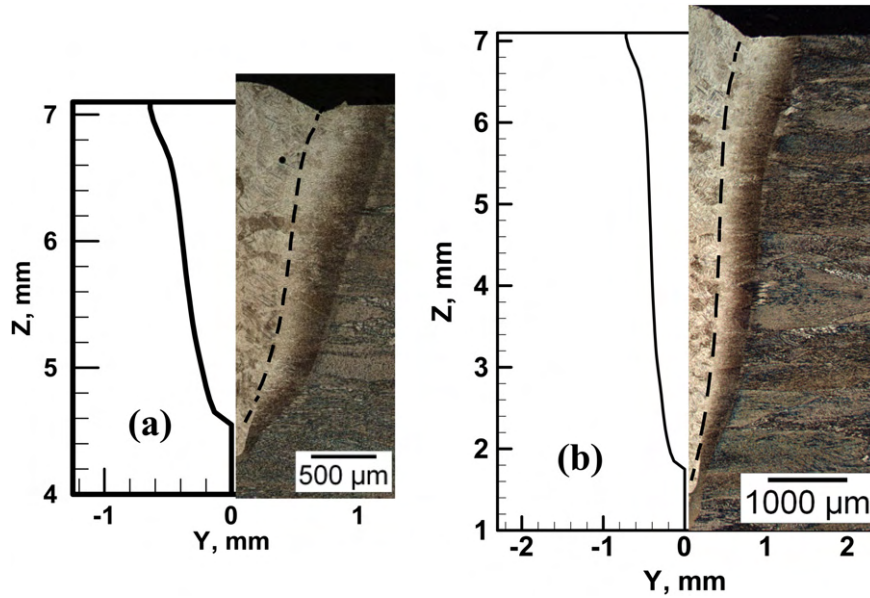$$\frac{\partial h}{\partial y} = 0. \tag{10}$$

Figure 2. The computed transverse fusion zone cross-sections shown by solid lines and the experimentally determined fusion zone cross-section for Ti–6Al–4V welds made at 16.9 mm s^{-1} welding speed with input power of (*a*) 550 W and (*b*) 1114 W shown by dotted lines.
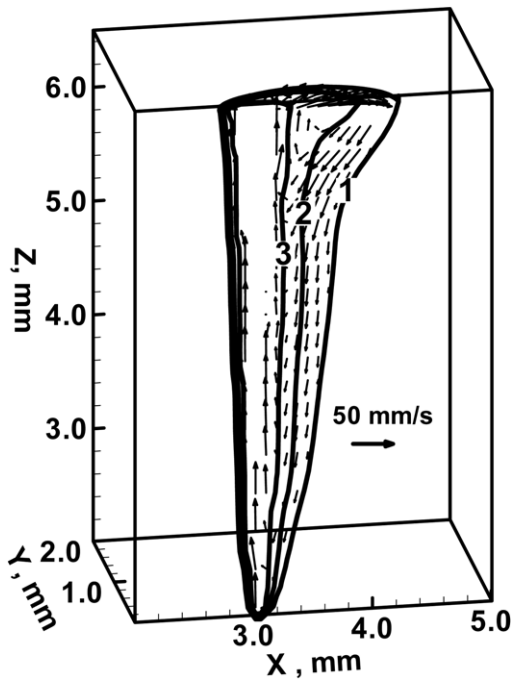

Figure 3. Fluid flow in a 21Cr–6Ni–9Mn stainless steel electron beam weld pool for 16.9 mm s^{-1} welding speed and 814 W input power. Levels 1, 2 and 3 correspond to temperatures 1697 K, 1900 K and 2200 K, respectively.

Keyhole surface.

$$h = h_{\text{boil}}, \tag{11}$$

where h_{boil} is the sensible heat of the different materials at their respective boiling points. The velocity component perpendicular to the keyhole surface is assigned zero to represent no mass flux due to convection. For the electron beam welds, surface tension gradients are present due to the variation of temperature on the keyhole surface with depth.
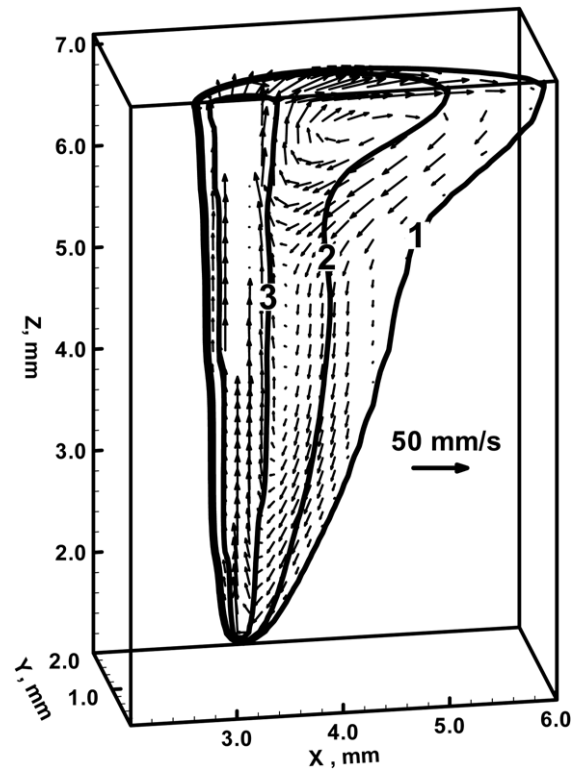

Figure 4. Fluid flow in a Ti–6Al–4V electron beam weld pool for 16.9 mm s^{-1} welding speed and 1114 W input power. Levels 1, 2 and 3 correspond to temperatures 1878 K, 2000 K and 2500 K, respectively.

As a result, Marangoni convection currents are formed in the vertical direction along the surface of the keyhole.

$$\mu \frac{\partial w}{\partial n} = \frac{\mathrm{d}\gamma}{\mathrm{d}T} \frac{\partial T}{\partial z}, \tag{12}$$

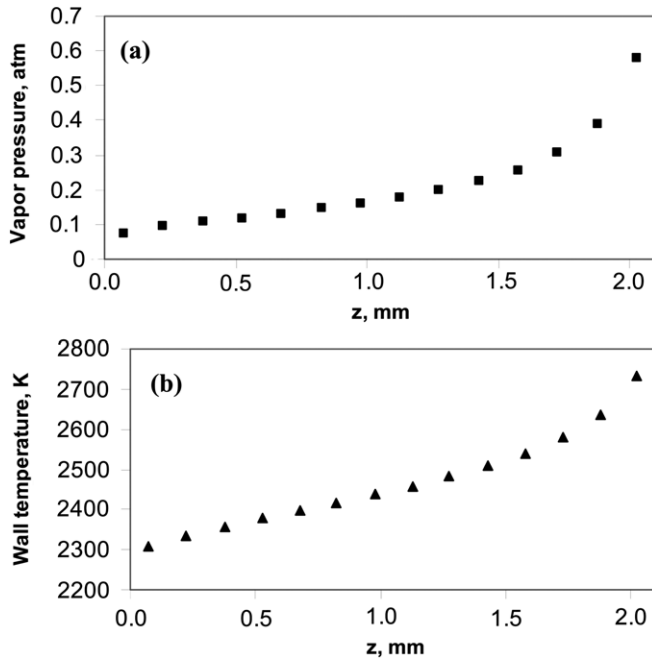where n is the direction vector normal to the keyhole surface.

Figure 5. Variation of (*a*) vapour pressure in the keyhole and (*b*) keyhole wall temperature, with depth for EBW of 21Cr–6Ni–9Mn stainless steel at 407 W input power and 16.9 mm s^{-1} welding speed. $z = 0$ at the surface of the workpiece.
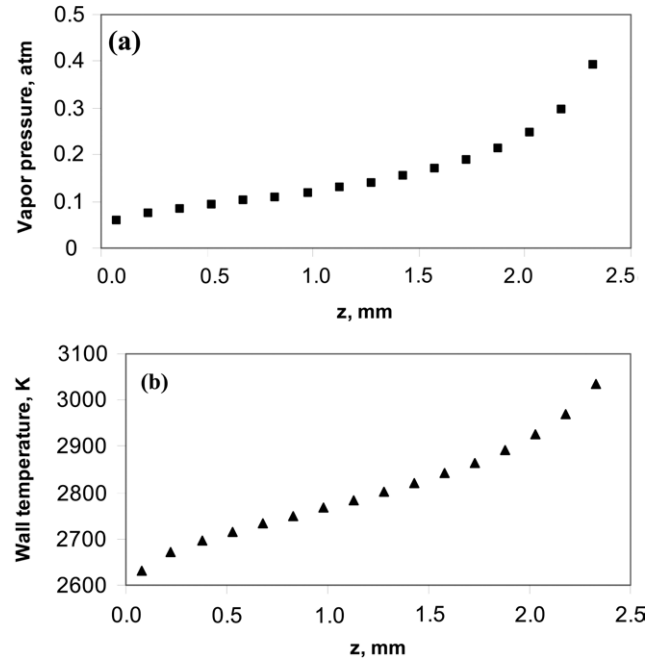

Figure 6. Variation of (*a*) vapour pressure in the keyhole and (*b*) keyhole wall temperature, with depth for EBW of Ti–6Al–4V at 550 W input power and 16.9 mm s^{-1} welding speed. $z = 0$ at the surface of the workpiece.

Solid surfaces. At all solid surfaces far away from the heat source, a convective heat transfer boundary condition is given and the velocities are set to be zero.

3.3. Turbulence model

During welding, the rates of transport of heat, mass and momentum are often enhanced because of the presence of fluctuating velocities in the weld pool. The contribution of the fluctuating velocities is taken into account by using an appropriate turbulence model that provides a systematic framework for calculating effective viscosity and thermal conductivity [58, 59]. The values of these properties vary with the location in the weld pool and depend on the local characteristics of the fluid flow. In this work, a turbulence model based on Prandtl's mixing length hypothesis is used to estimate the turbulent viscosity [58]:

$$\mu_t = \rho l_m v_t, \tag{13}$$

where μ_t is the turbulent viscosity, l_m is the mixing length and v_t is the turbulence velocity. The mixing length at any location within the weld pool is the distance travelled by an eddy before its decay and is often taken as the distance from the nearest wall [58]. In a controlled numerical study of recirculating flows in a small square cavity, the extent of computed turbulent kinetic energy was found to be about 10% of the mean kinetic energy [59]. Yang and DebRoy [60] computed mean velocity and turbulent energy fields during GMA welding of HSLA 100 steel using a two equation $k - \varepsilon$ model. Their results also show that the turbulent kinetic energy was of the order of 10% of the mean kinetic energy. The turbulent velocity v_t can therefore

be expressed as

$$v_t = \sqrt{0.1v^2}. \tag{14}$$

From equations (13) and (14), we have

$$\mu_t = 0.3\rho l_m v. \tag{15}$$

Effective viscosity at a particular point is given as the sum of the turbulent (μ_t) and laminar (μ_l) viscosities, i.e. $\mu = \mu_t + \mu_l$. The corresponding local turbulent thermal conductivities are calculated by using the turbulent Prandtl number, which is defined in the following relationship:

$$Pr = \frac{\mu_t c_p}{k_t}, \tag{16}$$

where k_t is the turbulent thermal conductivity. For the calculations described here, the Prandtl number is set to a value of 0.9, based on previous modelling work [57, 59], and the turbulent thermal conductivity is then calculated.

3.4. Calculation methodology

1. The keyhole geometry is calculated based on the energy balance at the liquid–vapour interface and the assumption of planar heat conduction, and keyhole wall temperatures are taken as the normal boiling point of the alloy [17].
2. The vapour pressure at any depth inside the keyhole is calculated from a force balance (see appendix) involving the vapour pressure, hydrostatic force, and surface tension force at the liquid–vapour interface.
3. Equilibrium pressure versus temperature relation for the given alloy is used to calculate the wall temperatures at all depths.

Table 3. Dimensionless numbers for EBW of 21Cr–6Ni–9Mn stainless steel at 814 W and Ti–6Al–4V at 1114 W, and the values used in calculations.

Dimensionless number	Definition	21Cr–6Ni–9Mn steel, 814 W	Ti–6Al–4V, 1114 W
Peclet number, Pe	$= \dfrac{u\rho C_p(w/2)}{k}$	8.4	7.3
Surface tension Reynold's number, Ma	$= \dfrac{\rho(w/2)|\mathrm{d}\gamma/\mathrm{d}T|\Delta T}{\mu^2}$	1.5×10^4	2.2×10^4
Reynold's number, *Re*	$= \dfrac{\rho u_{\mathrm{m}}w}{\mu}$	900	720
Magnetic Reynold's number, R_{m}	$= \dfrac{\rho \mu_{\mathrm{m}} I^2}{4\pi^2 \mu^2}$	2.5×10^{-4}	5.5×10^{-4}
Values used for calculations			
Characteristic flow velocity, m s^{-1}	u	0.1	0.1
Maximum flow velocity, m s^{-1}	u_{m}	1.0	0.6
Weld pool length, m	l	1.5×10^{-3}	3.0×10^{-3}
Weld pool width, m	w	9.0×10^{-4}	1.5×10^{-3}
Temperature difference*, K	ΔT	550	700
Density, kg m^{-3}	ρ	7000	4000
Viscosity, kg m^{-1} s^{-1}	μ	0.007	0.005
Thermal conductivity, W m^{-1} K^{-1}	k	30	30
Specific heat, J kg^{-1} K^{-1}	C_p	800	730
Surface tension, N m^{-1} K^{-1}	γ	1.87	1.65
Current, A	I	7.4×10^{-3}	10.4×10^{-3}
Magnetic permeability of free space, N A^{-2}	μ_{m}	$4\pi \times 10^{-7}$	$4\pi \times 10^{-7}$

Note: Difference between the calculated keyhole wall temperature near the top surface and solidus temperature.

4. Steps 1–3 are repeated a few times with improved values of wall temperatures. The iterations are stopped when the keyhole depth becomes constant with iterations.

5. The final keyhole geometry is mapped onto a coarser mesh for the solution of 3D mass, momentum, and energy balance equations. Temperatures within the keyhole at any depth are assigned the final wall temperature value calculated at that depth during keyhole geometry calculations.

6. The mass, momentum and energy conservation equations are solved assuming fixed wall temperatures and zero mass flux across the keyhole walls.

7. A turbulence model is used to enhance the viscosity and thermal conductivity in the liquid region.

4. Results and discussion

Figure 1 shows a comparison of computed and experimentally observed fusion zone cross-sections of two electron beam welds of 21Cr–6Ni–9Mn stainless steel for two input powers. The computed fusion zone cross-sections, shown by solid lines, are in very good agreement with the corresponding experimental results. Both welds show narrow and deep fusion zone geometry characteristic of electron beam welds. Figures 2(*a*) and (*b*) show a similar comparison of fusion zone cross-sections for Ti–6Al–4V welds at two different input powers. The fusion zones of the Ti–6Al–4V welds are characterized by columnar grains with a martensitic microstructure. A light etching inner HAZ and a dark etching outer HAZ can also be observed for the Ti–6Al–4V welds. The position of the fusion zone boundary at the top surface can be easily discerned by the deviation from the flat surface. Similarly, the fusion zone boundary can be discerned for

the 1114 W input power weld as well. The computed and experimental fusion zone cross-sections for both input powers are in excellent agreement. Note that the fusion zone cross-sections for the Ti–6Al–4V welds were much larger than those for the 21Cr–6Ni–9Mn welds. This difference is consistent with the much higher heat requirement for the melting of a unit volume of 21Cr–6Ni–9Mn than that of Ti–6Al–4V.

Figures 3 and 4 show the computed fluid flow for EBWs of 21Cr–6Ni–9Mn stainless steel and Ti–6Al–4V alloy welds, respectively. The fluid moving out from the centre of the weld pool carries heat and enhances the heat transfer. The region within the weld pool with no velocity vectors is the keyhole. On the keyhole walls, the velocity vectors due to Marangoni convection can be observed. These Marangoni convection currents bring heat from the keyhole bottom, where the wall temperature is relatively higher, to the surface and then outwards, thus enhancing the heat transfer within the weld pool. Such re-circulatory flow of hot liquid from the bottom to the top and then radially outwards, can result in increased weld pool width near the top surface.

Figure 5(*a*) shows the variation of vapour pressure with depth in the keyhole for the 21Cr–6Ni–9Mn stainless steel weld made with 407 W input power at 16.9 mm s^{-1}. The values given in the plot represent the pressure required to balance the surface tension force and the hydrostatic force of the liquid metal at the keyhole walls in order to keep the keyhole open. The metal–vapour pressure in the keyhole increases with depth and it can become very high near the keyhole bottom. As the keyhole radius becomes smaller with increasing depth, the pressure increases at a higher rate. In the calculation of keyhole profile, the radius of the keyhole decreases from a maximum value at the top to zero at the bottom. In reality, the keyhole bottom is likely to be rounded and the radius of curvature is
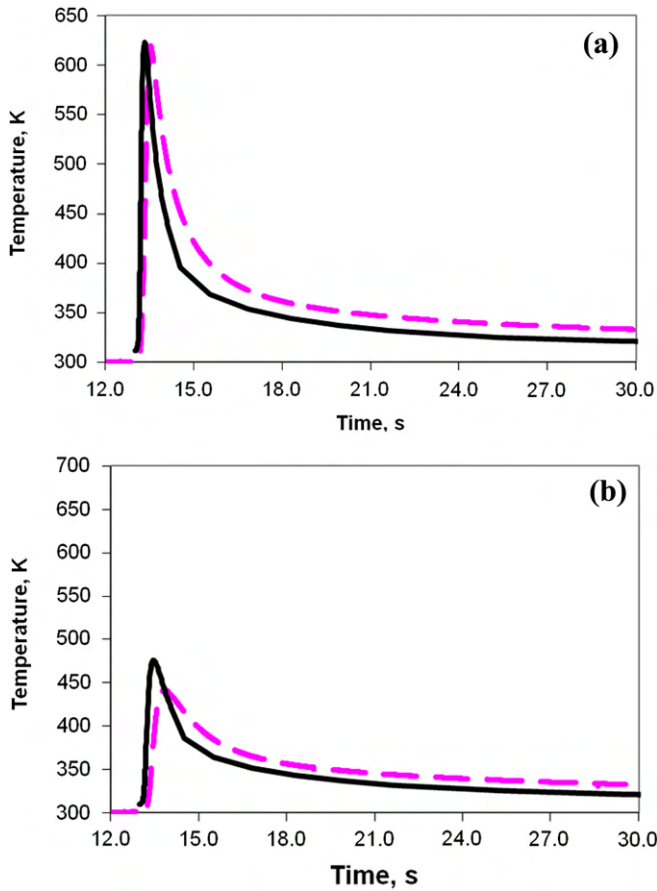
Figure 7. Experimental and computed thermal cycles for electron beam welds made on 21Cr–6Ni–9Mn stainless steel at 407 W input power and 16.9 mm s^{-1} welding speed at a location (*a*) 1.5 mm away from the weld centre line at the top surface and (*b*) 2.5 mm away from the weld centre line at the top surface. Solid lines show the computed thermal cycle.

Figure 8. Experimental and computed thermal cycles for electron beam welds made on 21Cr–6Ni–9Mn stainless steel at 814 W input power and 16.9 mm s^{-1} welding speed at a location (*a*) 1.5 mm away from the weld centre line at the top surface, (*b*) 2.5 mm away from the weld centre line at the top surface. Solid lines show the computed thermal cycle.

likely to have a finite value. Thus, calculated vapour pressures near the keyhole bottom may be somewhat higher than the true value.

Figure 5(*b*) shows the variation of wall temperature with depth and is calculated from the equilibrium pressure versus temperature relationship for 21Cr–6Ni–9Mn stainless steel. The equilibrium vapour pressures over the alloys were calculated assuming ideal solution behaviour. For example, for stainless steel, the equilibrium vapour pressure was taken as the sum of the products of the mole fraction and the equilibrium vapour pressure of pure Fe, Cr, Ni and Mn. The wall temperature varied by about 400 K from about 2308 K to about 2734 K. Figures 6(*a*) and (*b*) show the variation of keyhole pressure and wall temperature with depth for Ti–6Al–4V weld made with 550 W input power at 16.9 mm s^{-1} welding speed. The wall temperatures varied by about 400 K from 2632 K near the top surface to 3034 K near the keyhole bottom. Schauer and Giedt [29] measured the wall temperatures in an electron beam cavity for various alloys and found a similar variation with depth. As explained in the appendix, variation of keyhole wall temperatures with depth in laser beam welding is relatively small. Several prior works on modelling of keyhole mode laser welding have assumed constant keyhole wall
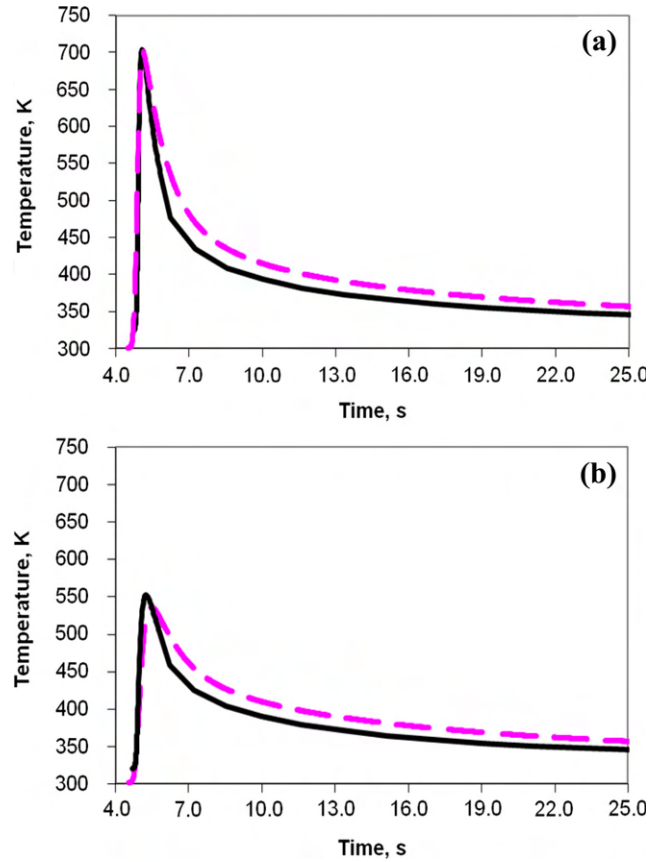
temperature [8, 10, 12, 17, 19]. Two-dimensional calculations of Trappe *et al* [61] also showed that keyhole wall temperatures in LBW were nearly constant.

Table 3 shows various dimensionless numbers calculated for the EBW of the two alloys and the values used in their calculation. Since the Peclet number is much higher than 1 for both the alloys, convection plays a very significant role in the heat transfer compared with conduction. Surface tension Reynold's number computed using the expression in table 3 for both alloys is of the order of 10^4 indicating strong influence of surface tension gradient on the fluid flow in comparison with the viscous force. According to Atthey's criteria [62], the weld pools are turbulent when Reynold's number $Re = \rho u_{\mathrm{m}} w/\mu > 600$, where ρ is the density, u_{m} is the maximum fluid velocity, w is the weld pool width and μ is the viscosity. Values in the table show that the condition is satisfied for the welding of both the materials indicating a turbulent weld pool. The very low value of magnetic Reynold's number indicates that the Lorentz force is insignificant compared with the viscous force.

Figures 7(*a*) and (*b*) provide a comparison of the computed and the experimentally determined temperature versus time plots at two monitoring locations for the welding of 21Cr–6Ni–9Mn steel. The time scales in the computed temperature versus time plots were constructed by dividing
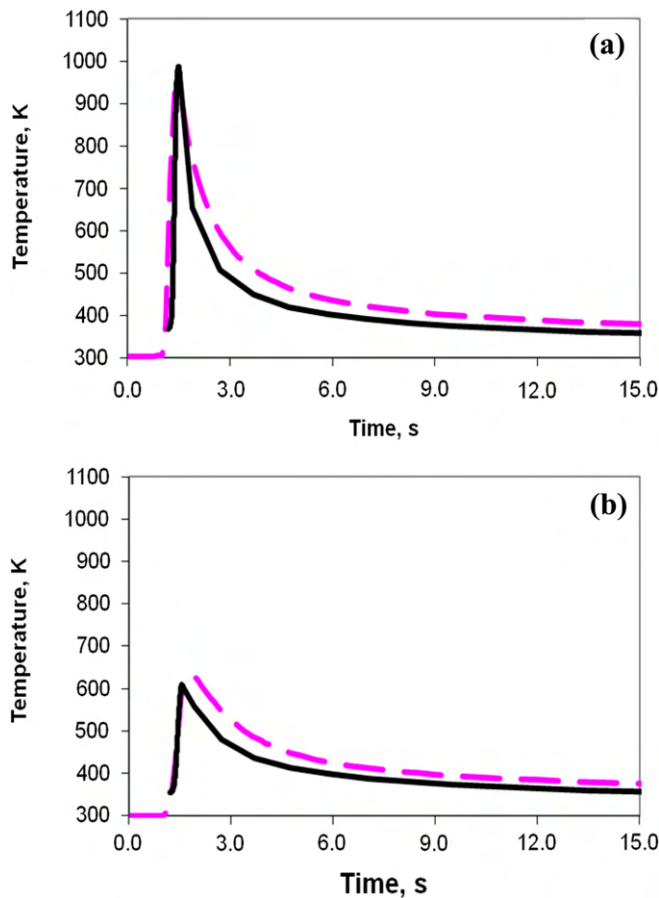
Figure 9. Experimental and computed thermal cycles for electron beam welds made on Ti–6Al–4V at 550 W input power and 16.9 mm s^{-1} welding speed at a location (*a*) 1.5 mm away from the weld centre line at the top surface, (*b*) 2.5 mm away from the weld centre line at the top surface. Solid lines show the computed thermal cycle.

Figure 10. Experimental and computed thermal cycles for electron beam welds made on Ti–6Al–4V at 1114 W input power and 16.9 mm s^{-1} welding speed at a location (*a*) 1.5 mm away from the weld centre line at the top surface, (*b*) 2.5 mm away from the weld centre line at the top surface. Solid lines show the computed thermal cycle.

the distance with the welding velocity. The experimental and the calculated time scales were synchronized by taking the same time to reach peak temperature for both plots. The computed thermal cycles agreed well with the corresponding experimentally determined values at both locations and for the location at the back of the plate (not shown). Figures 8(*a*) and (*b*) provide a comparison of the computed and the experimentally determined temperature versus time plots at the same monitoring locations and same welding conditions as before, except here the power was increased to 814 W. The computed thermal cycles agree well with the corresponding experimentally determined values for both locations shown in figure 8 and for a location at the back of the plate (not shown). A comparison of the data in figures 7 and 8 indicate that at any given monitoring location the peak temperature increases with increase in heat input.

Figures 9 and 10 show comparisons of the computed and the experimentally determined temperature versus time plots for Ti–6Al–4V at the same monitoring locations for two power levels. The computed thermal cycles agreed well with the corresponding experimentally determined values at the locations as shown in figures 9 and 10 as well as for a location at the back of the plate (not shown). The peak temperatures
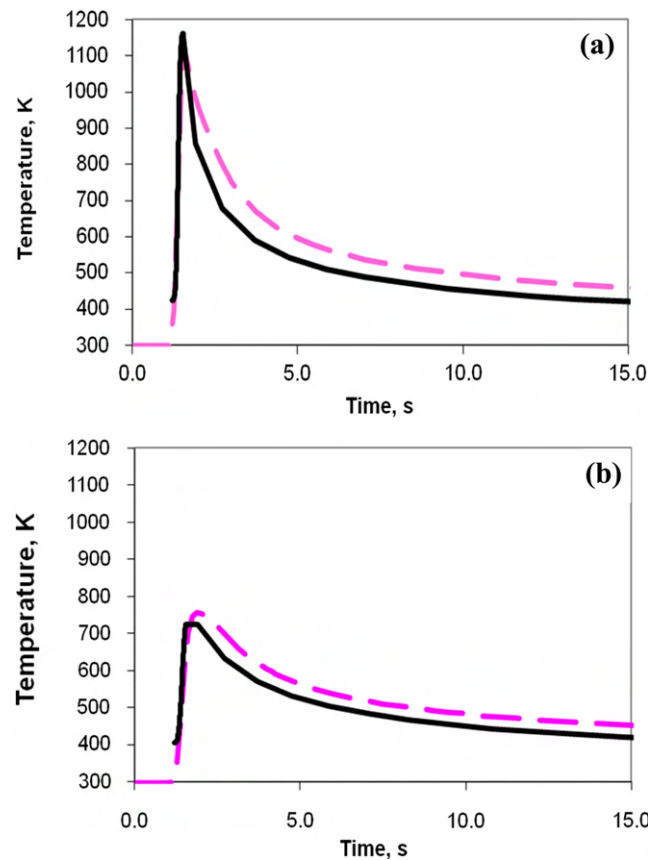
obtained at the top surface for Ti–6Al–4V made at 550 W were higher than the peak temperatures obtained at similar locations for 21Cr–6Ni–9Mn steel made at higher input power of 814 W. This can be attributed to the higher boiling point and lower solid state thermal conductivity of Ti–6Al–4V compared with 21Cr–6Ni–9Mn steel.

A comparison of calculated and experimental weld geometry for laser welds made on 21Cr–6Ni–9Mn stainless steel and Ti–6Al–4V alloy at 16.9 mm s^{-1} welding speed and 1500 W power setting are shown in figures 11 and 12, respectively. Microstructural features of the Ti–6Al–4V alloy laser weld are similar to those discussed previously for the electron beam welds on the same material. The agreement between the calculated position of the fusion boundary and the experimentally determined position for the 21Cr–6Ni–9Mn stainless steel weld is quite reasonable, while that for the Ti–6Al–4V alloy is very good. The weld geometry depends on the spot size of the beam and the beam distribution factor. The spot size and beam distribution factor measured under ideal conditions in the absence of any plasma can differ from the respective values in an actual experiment due to scattering and absorption phenomenon [45, 63, 64]. Therefore, the beam distribution factor and beam radius were adjusted to get a reasonable agreement between the experimental and calculated
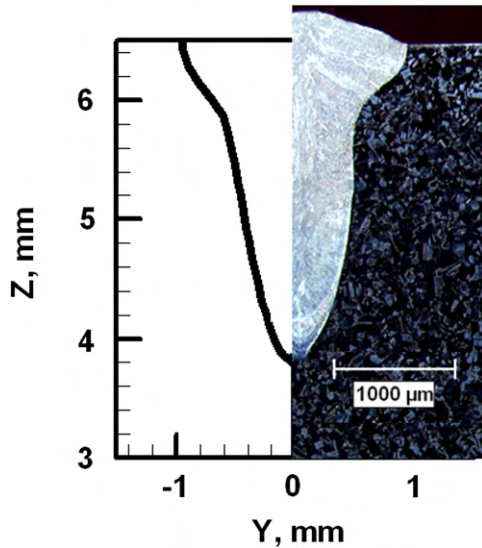
Figure 11. Experimental and calculated fusion zone cross-section for 21Cr–6Ni–9Mn stainless steel laser weld made at 16.9 mm s^{-1} welding speed, 1500 W input power and −1.27 mm beam defocus. The computed weld pool geometry is shown by the solid line.
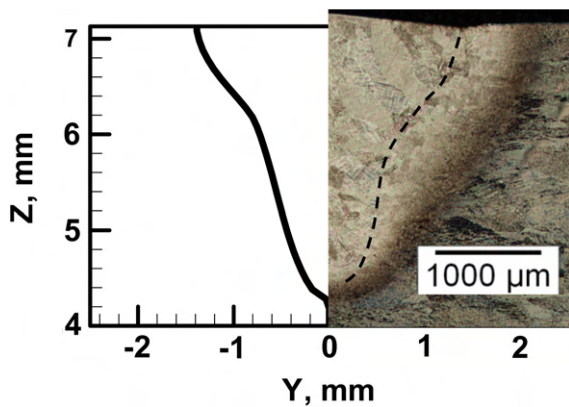

Figure 12. Experimental and calculated fusion zone cross-section for Ti–6Al–4V laser weld made at 16.9 mm s^{-1} welding speed and 1500 W input power. The computed cross-section is shown by the solid line and the experimentally determined fusion zone cross-section is shown by the dotted line.
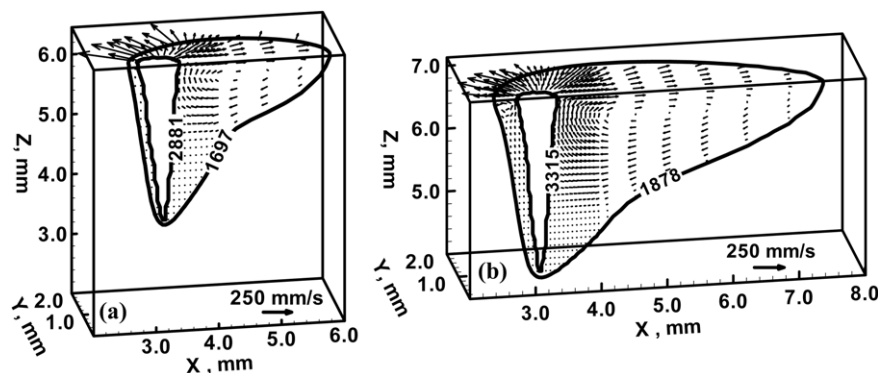
weld depth. The beam distribution factor and focal spot radius were taken as 1.5 and 0.23 mm for the calculations. Again, note that the fusion zone area for Ti–6Al–4V is distinctly larger than that for 21Cr–6Ni–9Mn stainless steel as expected from the previous discussions.

Figure 13 shows the fluid flow patterns during laser welding of 21Cr–6Ni–9Mn stainless steel and Ti–6Al–4V alloy welds made at 1500 W machine setting and 16.9 mm s^{-1} welding speed. In the absence of temperature gradients along the keyhole wall, there is no Marangoni convection along the keyhole walls in laser welds. For the conditions of experiments in this paper, 21Cr–6Ni–9Mn electron beam weld made at 16.9 mm s^{-1} welding speed and 814 W input power was deeper and narrower than the laser beam weld made on the same material at the same welding speed and 1500 W power. Similarly, the Ti–6Al–4V electron beam weld made at 16.9 mm s^{-1} welding speed and 1114 W input power was deeper and narrower than the laser beam weld on the same material at the same welding speed and 1500 W input power.

Figures 14 and 15 compare the calculated weld geometries for laser (14(*a*) and 15(*a*)) and electron beam (14(*b*) and 15(*b*)) welds on 21Cr–6Ni–9Mn stainless steel (figure 14) and Ti–6Al–4V alloy (figure 15). The calculations were performed for the same welding speed, input power, beam distribution factor, focal spot radius, beam divergence, absorption coefficient, and plasma attenuation coefficient. Therefore, the calculations considered only the effect of lower keyhole wall temperatures in EBW compared with LBW on the weld geometries. The lower wall temperatures required in EBW due to the lower ambient pressure enable deeper penetration compared with LBW. However, the higher wall temperatures in LBW result in greater heat conducted in any horizontal plane and consequently wider weld pools compared with EBW.

5. Summary and conclusions

An energy balance based model was used to calculate the keyhole shape in EBW by considering the variation of keyhole wall temperature as a function of keyhole depth. A numerical model was developed and tested to calculate the fluid flow and heat transfer during keyhole mode EBW of 21Cr–6Ni–9Mn
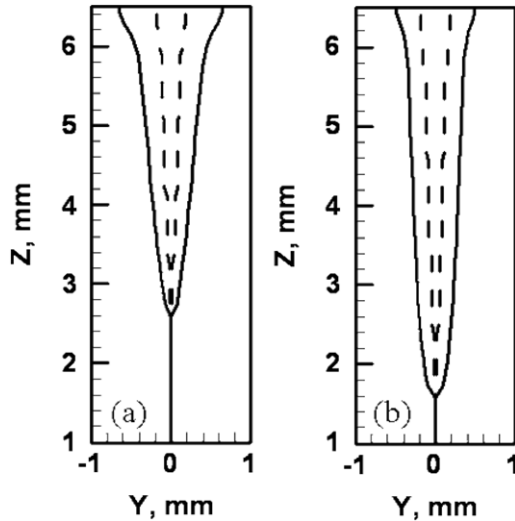

Figure 13. Fluid flow in the weld pool for laser welds for 1500 W machine power setting and 1.69 cm s^{-1} welding speed for (*a*) 21Cr–6Ni–9Mn stainless steel weld and (*b*) Ti–6Al–4V weld.

Figure 14. Computed fusion zone cross-sections for 21Cr–6Ni–9Mn stainless steel welds made with 1000 W input power at 17 mm s^{-1} welding speed by (*a*) LBW and (*b*) EBW.
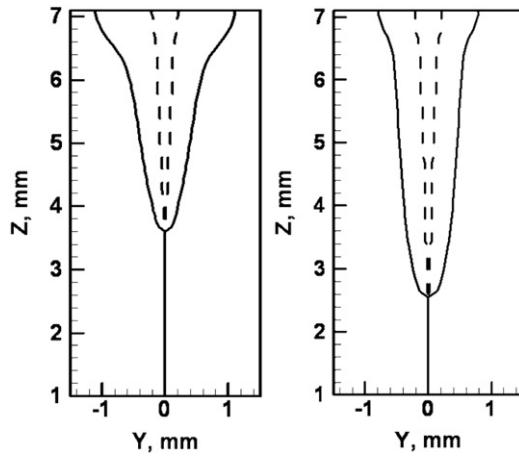

Figure 15. Computed fusion zone cross-sections for Ti–6Al–4V welds made with 1000 W input power at 17 mm s^{-1} welding speed by (*a*) LBW and (*b*) EBW.

stainless steel and Ti–6Al–4V alloy. The model was used to calculate temperature fields, thermal cycles, weld geometry, and fluid flow. A turbulence model based on Prandtl's mixing length hypothesis was used to estimate the effective viscosity and effective thermal conductivity values. Temperatures on keyhole walls in EBW were calculated from the equilibrium temperature–pressure relations for the metal–vapour interface. The vapour pressure, in turn, was calculated from a force balance on keyhole walls.

As expected, welding parameters such as the beam radius, input power, and welding speed affected the weld pool geometry. Relatively low keyhole wall temperature in EBW compared with that during LBW was a contributing factor in narrower electron beam welds for the experimental conditions considered here. The presence of surface tension driven vertical flow along the keyhole walls in EBW enhanced the heat transfer by convection. Calculation of dimensionless numbers showed that convection was the dominant mechanism of heat transfer in the weld pool, and the gradient of surface tension

played an important role in the fluid flow. The Lorentz force was insignificant compared with the Marangoni force. Higher peak temperatures found in Ti–6Al–4V welds compared with similar locations in 21Cr–6Ni–9Mn stainless steel welds was attributed to higher boiling point and lower solid state thermal conductivity of Ti–6Al–4V.

Acknowledgments

Appendix

The vapour pressure inside the keyhole tries to keep the vapour cavity open and both the surface tension and the hydrostatic forces tend to close the cavity. The force balance at the keyhole walls is given by

$$P = P_0 + \gamma(T)/r(z) + \rho g z, \qquad (A-1)$$

where P is the vapour pressure inside the keyhole, P_0 is the ambient pressure, $\gamma(T)$ is the surface tension at local wall temperature T, ρ is the density and g is the acceleration due to gravity. $r(z)$ is the average radius of curvature of the keyhole at distance z from the top surface, and is taken to be half of the keyhole diameter along the welding direction. Variation of vapour pressure with temperature can be given by integrating the Clausius–Clapeyron equation [16]:

$$P = P_0 \exp\left(H_{LV}\frac{T - T_{LV}}{RTT_{LV}}\right). \qquad (A-2)$$

In a typical EBW, $P_0 \sim 0$ atm, while in typical laser welding $P_0 \sim 1$ atm. From equation (A-2), an excess pressure (i.e. the pressure difference between the top and the bottom of the keyhole) of say, 0.5 atm, in an EBW cavity will result in temperature difference of several hundred degrees Kelvin. Since there is a continuous flow of metal vapours out of the keyhole, it can be assumed that the vapour cavity in LBW is filled with metal–vapour. Thus, for a similar excess pressure of 0.5 atm in the keyhole, the total vapour pressure due to metal atoms from the workpiece varies from 1 atm near the top of the keyhole to 1.5 atm near the keyhole bottom. The temperature difference between the bottom and the top of the LBW keyhole calculated from equation (A-2) will be much less than the corresponding value for electron beam welds.

Temperature at all locations on the keyhole walls in LBW is commonly assumed to be equal to the boiling point of the alloy [16]. However, the larger variation of temperature on the keyhole walls for EBW has been considered during the calculation of keyhole geometry and also for the surface tension gradient (resulting from temperature dependence of surface tension) driven Marangoni convection along the keyhole walls.

References

[1] DebRoy T and David S A 1995 *Rev. Mod. Phys.* **67** 85–116
[2] David S A and DebRoy T 1992 *Science* **257** 497–502
[3] Klein T, Vicanek M, Kroos J, Decker I and Simon G 1994 *J. Phys. D: Appl. Phys.* **27** 2023–30
[4] Swift-Hook D E and Gick A E F 1973 *Weld. J. (Miami)* **52** 492s–9s
[5] Andrews J G and Atthey D R 1976 *J. Phys. D: Appl. Phys.* **9** 2181–94
[6] Klemens P G 1976 *J. Appl. Phys.* **47** 2165–74
[7] Mazumder J and Steen W M 1980 *J. Appl. Phys.* **51** 941–7
[8] Dowden J, Postacioglu N, Davis M and Kapadia P 1987 A keyhole model in penetration welding with a laser *J. Phys. D: Appl. Phys.* **20** 36
[9] Kroos J, Gratzke U and Simon G 1993 *J. Phys. D: Appl. Phys.* **26** 474–80
[10] Ye X H and Chen X 2002 Three-dimensional modelling of heat transfer and fluid flow in laser full-penetration welding *J. Phys. D: Appl. Phys.* **35** 1049
[11] Sudnik W, Radaj D and Erofeew W 1996 *J. Phys. D: Appl. Phys.* **29** 2811–7
[12] Matsunawa A and Semak V 1997 *J. Phys. D: Appl. Phys.* **30** 798–809
[13] Solana P and Ocana J L 1997 *J. Phys. D: Appl. Phys.* **30** 1300–13
[14] Ki H, Mohanty P S and Mazumder J 2002 *Metall. Mater. Trans.* A **33** 1817–30
[15] Ki H, Mohanty P S and Mazumder J 2002 *Metall. Mater. Trans.* A **33** 1831–42
[16] Lee J Y, Ko S H, Farson D F and Yoo C D 2002 *J. Phys. D: Appl. Phys.* **35** 1570–6
[17] Kaplan A 1994 *J. Phys. D: Appl. Phys.* **27** 1805–14
[18] Pastor M, Zhao H, Martukanitz R P and DebRoy T 1999 *Weld. J.* **78** 207s–16s
[19] Zhao H and DebRoy T 2003 *J. Appl. Phys.* **93** 10089–96
[20] Rai R and DebRoy T 2006 *J. Phys. D: Appl. Phys.* **39** 1257–66
[21] Rai R, Roy G G and DebRoy T 2007 *J. Appl. Phys.* **101** 054909
[22] Rai R, Kelly S M, Martukanitz R P and DebRoy T 2008 *Metall. Mater. Trans.* A **39** 98–112
[23] Rai R, Elmer J W, Palmer T A and DebRoy T 2007 *J. Phys. D: Appl Phys* **40** 5753–66
[24] Wei P S and Geidt W H 1985 *Weld. J.* **64** 251s–9s
[25] Elmer J W, Giedt W H and Eagar T W 1990 *Weld. J.* **69** 167s–76s
[26] Wei P S and Chow Y T 1992 *Metall. Trans.* B **23** 81–90
[27] Ho C Y, Wen M Y and Lee Y C 2008 *Vacuum* **82** 316–20
[28] Hemmer H and Grong O 1999 *Sci. Technol. Weld. Joining* **4** 219–25
[29] Schauer D A, Giedt W H and Shintaku S M 1978 *Weld J.* **57** 127s–33s
[30] Schiller S, Heisig U and Panzer S 1982 *Electron Beam Technology* (Berlin: Wiley)
[31] Brandes E A and Brook G B (ed) 1992 *Smithells Metals Reference Book* 7th edn (Boston, MA: Butterworth–Heinemann)
[32] Turkdogan E T 1980 *Physical Chemistry of High Temperature Technology* (New York: Academic)
[33] Ho C Y, Liley P E and Power R W 1968 National Bureau of Standards *National Standard Reference Data Series: No 16: Thermal Conductivity of Selected Materials* Part 2 (Washington DC: USGPO)
[34] Lide D R (ed) 2000 *CRC Book of Chemistry and Physics* 81st edn (Boca Raton, FL: CRC Press)
[35] He X, Elmer J and DebRoy T 2005 *J. Appl. Phys.* **97** 84909
[36] Yaws C L 1997 *Handbook of Thermal Conductivity* (Houston, TX: Gulf)
[37] Iida T and Roderick Guthrie I L 1988 *The Physical Properties of Liquid Metals* (Oxford: Clarendon)
[38] Mills K C 2002 *Recommended Values of Thermophysical Properties of Selected Commercial Alloys* (Materials Park, OH: ASM)
[39] Kaye G W C and Laby T B 1995 *Tables of Physical and Chemical Constants* (London: Longman)
[40] Ho C Y and Touloukian Y S 1977 Purdue University Thermophysical Properties Research Centre, TPRC data series *Thermophysical Properties of Matter: Thermal Conductivity* (New York: Plenum)
[41] Mishra S and DebRoy T 2004 *Acta Mater.* **52** 1183–92
[42] Tix C and Simon G 1993 *J. Phys. D: Appl. Phys.* **26** 2066–74
[43] Yilbas B S, Yilbas Z and Akcakoyun N 1996 *Opt. Laser Techol.* **28** 503–11
[44] Dilthey U, Goumeniouk A, Lapota V and Turichin G 2000 *J. Phys. D: Appl. Phys.* **33** 2747–53
[45] Dilthey U, Goumeniouk A, Nazarenko O K and Aktopjatz K S 2001 *Vacuum* **62** 87–96
[46] Bird R B, Stewart W E and Lightfoot E N 1960 *Transport Phenomena* (New York: Wiley)
[47] Patankar S V 1980 *Numerical Heat Transfer and Fluid Flow* (New York: Hemisphere)
[48] Voller V R and Prakash C 1987 *Int. J. Heat Mass Transfer* **30** 1709–19
[49] Brent A D, Voller V R and Reid K J 1988 *Numer. Heat Transfer* **13** 297–318
[50] Zhang W, Kim C H and DebRoy T 2004 *J. Appl. Phys.* **95** 5210–9
[51] Zhang W, Kim C H and DebRoy T 2004 *J. Appl. Phys.* **95** 5220–9
[52] Kumar A and DebRoy T 2003 *J. Appl. Phys.* **94** 1267–77
[53] Kou S and Sun D K 1985 *Metall. Trans.* A **16** 203–13
[54] Kim C H, Zhang W and DebRoy T 2003 *J. Appl. Phys.* **94** 2667–79
[55] De A and DebRoy T 2004 *J. Phys. D: Appl. Phys.* **37** 140–50
[56] De A and DebRoy T 2004 *J. Appl. Phys.* **95** 5230–40
[57] Wilcox D C 1993 *Turbulence Modeling for CFD* (La Canada, CA: DCW Industries)
[58] Launder B E and Spalding D B 1972 *Lectures in Mathematical Models of Turbulence* (London: Academic)
[59] Hong K 1996 *PhD Thesis* University of Waterloo pp 145
[60] Yang Z and DebRoy T 1999 *Metall. Trans.* B **30** 483–93
[61] Trappe J, Kroos J, Tix C and Simon G 1994 On the shape and location of the keyhole in penetration laser-welding *J. Phys. D: Appl. Phys.* **27** 2152
[62] Atthey D R 1980 *J. Fluid Mech.* **98** 787–801
[63] Miller R and DebRoy T 1990 *J. Appl. Phys.* **68** 2045–50
[64] Collur M M and DebRoy T 1989 *Metall. Trans.* B **20** 277–85